

# Frequency-Multiplexed Transmitted-Wave Manipulation with Multifunctional Acoustic Metasurfaces

Haoyi Cheng<sup>1</sup>, Jingwen Guo<sup>1</sup>, Xin Zhang<sup>1</sup>, and Wenjing Ye<sup>1\*</sup>

*Department of Mechanical and Aerospace Engineering, The Hong Kong University of Science and Technology, Clear Water Bay, Kowloon, Hong Kong, China*



(Received 26 April 2023; revised 15 July 2023; accepted 2 August 2023; published 6 September 2023)

Passive metasurfaces are known for their fixed and usually single-wave manipulation functionality, which limits their potential applications for diverse scenarios. To expand the functionality of the passive metasurfaces, frequency-multiplexed technology has been proposed to encode multiple operation frequencies in a single metasurface for function selection and switching. Although this technology has been extensively utilized for electromagnetic waves, there have been few studies on designing frequency-multiplexed metasurfaces for acoustic-wave manipulation. This work applies a topology optimization method based on a multiobjective genetic algorithm (GA) to develop different frequency-encoded multifunctional acoustic metasurfaces to attain acoustic focusing and anomalous wave refraction. The effectiveness of the optimized metasurfaces is validated both numerically and experimentally. Additionally, the underlying physical mechanisms of the designed frequency-multiplexed acoustic metasurfaces are systematically analyzed. This study presents high-performance frequency-multiplexed metasurfaces for acoustic-wave-front modulation and demonstrates the promising potential of the GA-based topology optimization approach in designing integrated, miniaturized multifunctional acoustic devices for real-world applications.

DOI: [10.1103/PhysRevApplied.20.034009](https://doi.org/10.1103/PhysRevApplied.20.034009)

## I. INTRODUCTION

Acoustic metamaterials are artificial materials that possess novel physical properties and unique functionalities unattainable by natural materials. Among them, acoustic metasurfaces have attracted a great deal of attention in recent decades because of their subwavelength thickness. Their unique wave manipulation capabilities and compact sizes make them excellent candidates in a wide range of potential practical applications involving wave-front modulation. Examples include, but are not limited to: manipulation of three-dimensional (3D) multiscale particles or molecules [1–3]; super-resolution medical imaging [4,5]; tumor ablation with high-intensity focused ultrasound [6,7] and nerve stimulation with low-intensity focused ultrasound [8,9] in biomedical testing and clinical treatment; acoustic trapping volumetric display [10,11] and virtual tactile sensing [12,13] for virtual reality and human-computer interaction in the prospective “Metaverse” age; multiple-input and multiple-output signal processing devices [14,15]; surface-acoustic-wave signal filtering [16,17]; information-encrypted wireless communication systems [18]; and automated nondestructive testing systems [19].

The field of acoustic metamaterials has developed rapidly in recent years, and a variety of metamaterials with different functionalities have been designed and demonstrated, for example, metadevices for noise reduction [20], perfect absorption [21,22], carpet cloaking [23,24], sound diffusing [25,26], acoustic focusing [27,28], anomalous reflection and refraction [29,30], and vortex beam generation [31,32]. Typically, these acoustic metasurfaces consist of an array of unit cells with different microstructures, such as space-coiling structure [33,34], labyrinthine structure [35,36], thin membrane [37,38] and Helmholtz resonator [39,40]. Most of these metasurfaces are passive and have a fixed wave function operated at a single frequency. The limited and fixed function dramatically limits the application scope of these devices.

To increase the functionality and retain passivity, frequency-multiplexed acoustic metasurfaces have been proposed in which multiple functions have been realized in passive metasurfaces using operation frequency as a tunable degree of freedom. Compared to reflection-type multiplexed metasurfaces, the transmission-type multiplexed metasurfaces are much more challenging to optimize and design. To date, only a few studies have been conducted. Brown *et al.* [41] realized three-frequency acoustic kinoforms which can project pre-encoded images on three different axial focal planes at three working frequencies. These kinoforms are essentially phase plates,

\*mewye@ust.hk

which are bulky and have a relatively low efficiency. Zhu *et al.* [42] used Fabry–Pérot (FP) resonant channels to design two-frequency-multiplexed transmission-type acoustic metaholograms. Zhang *et al.* [43] realized two-frequency-multiplexed acoustic functions on coding metasurfaces using two-layer Helmholtz-type resonators. Most of these designs either realize only two functions or have a relatively large size and a low efficiency. To push for high performance, it is desirable to increase the functionalities while keeping the element and/or device compact. In addition, high transmission is also required in many practical applications.

The design of high-performance frequency-multiplexed metamaterials requires a design approach that can handle multiple design objectives and constraints. Currently, the design of acoustic metamaterials mostly follows a physics-driven, “top-down” approach in which the design starts with a preselected mechanism, for example, local resonance, and a fixed structural topology, and then proceeds with a parametric optimization on the fixed topology to obtain the desired material properties. These approaches are easy to implement, but it is difficult to incorporate multiple objectives and constraints into them due to the limited number of design degrees of freedom.

Recently, inverse design approaches based on topology optimization (TO) have been increasingly applied to the design and optimization of mechanical metamaterials [44,45], elastic metamaterials [46,47], and acoustic metamaterials [48–52]. Examples include sound cloaking [48] and an acoustic diode [49] designed using a density-based TO method, acoustic metasurfaces for reflective beam steering and wave focusing designed via a level-set-based TO method [50], underwater acoustic absorption [51], and broadband two-bit coding metasurfaces [52] designed using a TO combined with single-objective genetic algorithm (GA). One distinct feature in TO-based design approaches is that the working mechanism and the topology of the design rarely need to be specified *a priori*. The most suitable mechanisms and the optimal topological configurations are formed naturally through the inverse design process. Thus, the design degrees of freedom become much larger, allowing metadevices with complex functionalities to be designed.

In this paper, we utilize the multiobjective topology optimization framework for systematic design of sub-wavelength, transmission-type metasurfaces for achieving dual-frequency- and triple-frequency-multiplexed wave focusing and function switching. In practice, frequency-multiplexed and multifunctional acoustic metasurfaces have many significant application scenarios, for instance, integrated multifunctional components (high-resolution multiscale 3D imaging [53], interactive 3D naked-eye display [54], and photoacoustic devices [55]), miniaturized acoustic devices, and large-scale underwater communica-

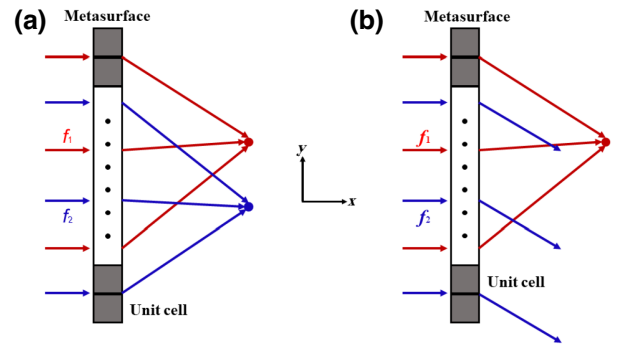


FIG. 1. Schematic diagram of frequency-multiplexed metasurfaces: (a) frequency-multiplexed acoustic-wave focusing, and (b) frequency-multiplexed acoustic function switching.

## II. DESIGN METHODOLOGY

### A. Design principle

The target of the present study is to design acoustic metasurfaces that have different wave manipulation functions at different operation frequencies. We select wave focusing and beam steering to focus on, because they are the basic functions required in acoustic imaging, particle levitation, orientational detection antennas, and object perception. Figure 1 presents a schematic diagram of the two specific two-dimensional design cases considered in this work, which are coplanar wave focusing and function switching between wave focusing and beam steering at different frequencies.

According to the Huygens-Fresnel principle [56] and the general Snell’s law (GSL) [57], wave-front modulation can be realized by a metasurface that possesses a specific phase profile as shown in Eq. (1):

$$k_0(\sin \theta_t - \sin \theta_i) = \frac{d\phi(y)}{dy}. \quad (1)$$

Based on Eq. (1), the specific phase profiles required for wave focusing and anomalous refraction for a normally incident plane wave can be derived, which are shown in Eqs. (2) and (3), respectively:

$$\phi(y) = k_0(\sqrt{(y - y_d)^2 + F^2} - F), \quad (2)$$

$$\frac{d\phi(y)}{dy} = k_0 \sin \theta_t = \text{constant}. \quad (3)$$

Here  $k_0 (= 2\pi/\lambda)$ , with  $\lambda$  being the wavelength) is the wave number of the incident and transmitted wave at operation frequency;  $\theta_i$  and  $\theta_t$  represent the incident angle and refracted angle, respectively;  $\phi(y)$  is the phase shift produced by the metasurface, which is a function of the location along the  $y$  direction as shown in Fig. 1;  $F$  denotes the focal length, that is, the horizontal distance between the focal point and the metasurface; and  $(F, y_d)$  are the

coordinates of the desired focal point at the corresponding operation frequency.

### B. Topology optimization based on the nondominated sorting genetic algorithm (NSGA-II)

Topology optimization refers to an effective method to explore the optimal materials distribution inside a design domain to maximize (or minimize) the design objectives. The density-based TO method is employed in this work. The design domain of the unit cell is specified according to the size requirements, and then is discretized into a set of  $20 \times 20$  uniform elements (400 design variables). Each element (pixel) is assigned a material index to indicate different physical properties of the corresponding material. The optimization process is to find the optimal value of the material index of each element, so that the topological structure can achieve the design objectives while satisfying the constraints. In this work, two related physical properties, density ( $\rho$ ) and bulk modulus ( $K$ ), of each pixel can be represented as

$$\rho(\mathbf{r}) = (\rho_2 - \rho_1)\epsilon(\mathbf{r}) + \rho_1, \quad (4)$$

$$K(\mathbf{r}) = (K_2 - K_1)\epsilon(\mathbf{r}) + K_1. \quad (5)$$

Here  $\rho_1$  and  $\rho_2$  denote the densities of the two different materials; and  $K_1$  and  $K_2$  are the different bulk moduli. Finally,  $\epsilon(\mathbf{r})$  represents the material index, which is a 0 or 1 representation. Index 0 represents air ( $\rho_{\text{air}} = 1.21 \text{ kg/m}^3$ ,  $c_{\text{air}} = 343 \text{ m/s}$ ,  $K_{\text{air}} = 149\,124 \text{ Pa}$ ), and 1 represents solid material, the photosensitive resin ( $\rho_{\text{solid}} = 1050 \text{ kg/m}^3$ ,  $c_{\text{solid}} = 2300 \text{ m/s}$ ,  $K_{\text{solid}} = 5.08 \times 10^9 \text{ Pa}$ ). Because the acoustic impedance of the resin is much larger than that of air, the photosensitive resin can be assumed as an acoustically hard medium.

To realize multiple acoustic functions at different target frequencies, a metasurface needs to produce distinct phase shifts independently when acoustic waves of different frequencies are normally incident onto it. In addition, for high-performance transmission-type metasurfaces, it is necessary to guarantee high energy transmission. Because of the multiple competing objectives and the highly non-convex nature of the design, one gradient-free method, the nondominated sorting genetic algorithm (NSGA-II) [58] is chosen to solve the optimization problem. This method performs a stochastic search in the entire design domain without requiring a good initial structure and is less likely to be trapped in a local minimum. And in a typical binary-coded GA-based TO, there is no intermediate density, eliminating the issue of grayscale region. Moreover, this algorithm is suitable for design with multiple objectives and constraints, allowing automatic searching for an optimal solution that can balance all objectives and constraints [59].

The optimization starts with an initial population  $N_p = 100$  of binary structures generated randomly. The volume fraction of the solid in the initial population is set to be 0.5. The ‘‘abuttal entropy filter’’ is adopted on each individual to alleviate the checkerboard problem and improve topology effectiveness. Next, the fitness is evaluated with transmission coefficient and phase shift calculated by the method discussed in the next subsection. The NSGA-II operations, including tournament selection, step-change crossover (reduce 0.02 per 200 generations), and uniform mutation, are then conducted sequentially to produce an offspring generation: First, select the best individual from the tournament groups with four random parent chromosomes based on fitness to generate a crossover pool (50 chromosomes). Second, then each individual has a crossover probability  $P_c = 0.9$  to enlarge the gene bank. Third, a probability  $P_m = 0.1$  is used for mutation (alter the representative value of 40 pixels) to obtain an offspring generation with 100 chromosomes. Fourth, finally, assemble the parent and offspring generations (total 200 individuals) for elite strategy and produce a new parent generation, which can retain an elite individual as much as possible and accelerate the whole evolution process robustly. The procedure is executed iteratively until the number of generations or the average residual error reaches the corresponding prescribed value.

### C. Objective functions

Besides a high transmission coefficient and required phase-shift profiles, to construct a practical multifunctional acoustic metasurface, the constraints on the topological structure are also formulated into our design objectives. The goal is to avoid isolated elements, small solid blocks, and extremely thin air channels that cause significant viscous dissipation, so guaranteeing sufficient strength and robust acoustic characteristics. All the above constraints and requirements of metasurface unit-cell design can be formulated as follows:

$$\text{objective}_1 = \min \sum_{k=1}^j |T_k - 1|, \quad (6)$$

$$\text{objective}_2 = \min \sum_{k=1}^j \frac{|\phi - \phi_{\text{desired}}|}{\pi}, \quad (7)$$

$$\text{objective}_3 = \min(\alpha N_{dc} + \beta N_{db} + \gamma N_{sm}). \quad (8)$$

Here  $T_k$  and  $\phi$  denote the transmission coefficient and phase shift corresponding to the incident wave of the  $k$ th target frequency;  $j$  represents the total number of operation frequencies; and  $\phi_{\text{desired}}$  represents the required phase profile calculated from Eqs. (2) and (3). In addition,  $\alpha$  and  $\beta$  are the penalty factors for the number and the total area of isolated pixels ( $N_{dc}$ ) and disconnected small

solid blocks ( $N_{db}$ ), respectively, which encourage the disconnected solid components to be no smaller than five elements; and  $\gamma$  is defined as the penalty parameter for the small elements ( $N_{sm}$ ) connected to the top and bottom hard boundaries. In this work, these three are set as  $\alpha = 0.25$ ,  $\beta = 0.05$ , and  $\gamma = 0.05$ .

Compared to single-objective GA methods, the multiobjective GA approach employs the concept of ‘‘Pareto optimality’’, which defines a high-efficiency situation in which no single improvement can be achieved at the expense of deteriorating the others [60]. Thus, the fitness function can be simply defined as a summation of all the objective functions without manually prioritizing objective functions and is formulated as follows:

$$\text{fitness} = \text{objective}_1 + \text{objective}_2 + \text{objective}_3. \quad (9)$$

The penalty factors in Eq. (8) are selected so that all objectives in Eq. (9) have roughly the same scale. Although fixed values are used in this work, they can be tuned during the optimization process to balance the acoustic characteristics performance and topology structure robustness for corresponding practical applications.

Figure 2 provides the evolution process of the best individual in some generations. In the first several tens of generations, the GA maintains a high level of diversity and dramatically reduces the disconnected structures. Afterwards, it gradually improves the phase shift and transmission coefficient with delicate tuning of beneficial topology structures. The number of iterations for all two-frequency-multiplexed designs is the range of (500, 600). As for the three-frequency-multiplexed unit cells, the total number of evolutionary generations vary from 300 to 800.

#### D. Numerical simulation setup

Throughout this paper, the full-field wave simulation is based on the Pressure Acoustic Module of COMSOL Multiphysics software. As shown in Dong [61], thermal-viscous losses are notable in long narrow air channels, but not so significant in short channels. The spatial dimensions of our predefined design domain are small compared with the operation wavelengths, hence it is expected that thermal-viscous effects would play an insignificant role in the performance of the designed metasurfaces.

The numerical simulation setup for each unit cell is shown in Fig. 3, the width of the simulation domain  $w = 0.05$  m, and the thickness of a unit cell  $t = 0.05$  m. The mesh size is fixed at 2.5 mm, which is close to  $\lambda/30$  of the shortest wavelength. Perfectly matched layers (PML) are set at both ends to absorb reflected waves. The sound plane wave is radiated from the background sound field (pressure amplitude is defined as 1 Pa). A plane wave with an amplitude of 1 Pa is radiated from the left of the unit cell. Both the top and bottom boundaries of the air domain are set as Floquet periodic conditions. An acoustically hard wall is

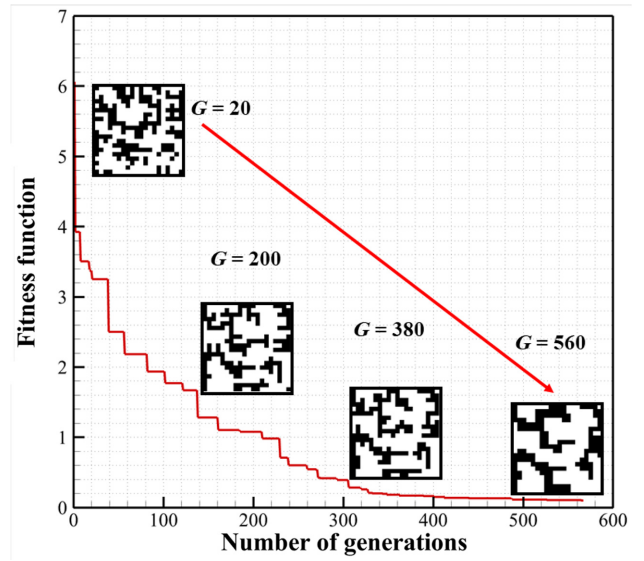


FIG. 2. Evolution process of unit cell no. 2 of a two-frequency-multiplexed acoustic focusing metasurface (the insets show the best individual at different generations,  $G$ ).

applied on the top and bottom boundaries of the unit cell to avoid crosstalk between two adjacent units. There are four monitors placed upstream and downstream of the air domain to extract the sound-field characteristics.

Based on all this, the transmission coefficient and phase shift are calculated as [62]

$$A = \frac{i(P_1 e^{ik_0 \cdot x_2} - P_2 e^{ik_0 \cdot x_1})}{2 \sin k_0 (x_1 - x_2)}, \quad (10)$$

$$B = \frac{i(P_2 e^{-ik_0 \cdot x_1} - P_1 e^{-ik_0 \cdot x_2})}{2 \sin k_0 (x_1 - x_2)}, \quad (11)$$

$$C = \frac{i(P_3 e^{ik_0 \cdot x_4} - P_4 e^{ik_0 \cdot x_3})}{2 \sin k_0 (x_3 - x_4)}, \quad (12)$$

$$D = \frac{i(P_4 e^{-ik_0 \cdot x_3} - P_3 e^{-ik_0 \cdot x_4})}{2 \sin k_0 (x_3 - x_4)}, \quad (13)$$

$$T = |C/A|, \quad (14)$$

$$\phi = \arg(C/A). \quad (15)$$

Here  $x_1, x_2, x_3$ , and  $x_4$  are the  $x$  coordinates of the four monitors indicated in Fig. 3; and  $P_1, P_2, P_3$ , and  $P_4$  represent the complex sound pressure at these four locations. In addition,  $A, B, C$ , and  $D$  denote the transmitted and reflected

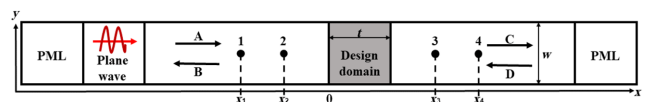


FIG. 3. Schematic diagram of the simulation model for an acoustic wave propagating through a unit cell.

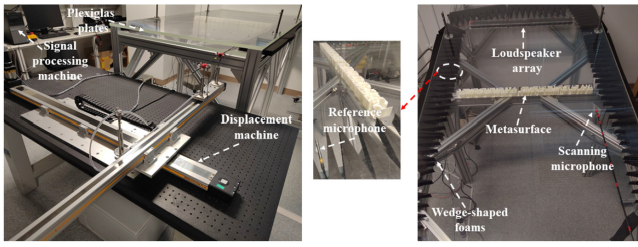


FIG. 4. Photographs of the acoustic test rig and the associated measurement equipment.

complex sound pressures of the incident, reflected, transmitted, and backward-transmitted sound fields.

### E. Fabrication and experimental measurement

To verify the effectiveness and performance of our designed multifunctional metasurfaces, the transmitted acoustic fields of the dual-frequency-multiplexed metasurfaces are experimentally measured using an in-house acoustic test rig. Each metasurface contains sixteen unit cells fabricated via stereolithography using a UnionTech Lite800HD printer (Wenext) with a photosensitive resin that has the same physical properties as those used in the simulation. The printing resolution of test samples is 0.2 mm, which is sufficient for the configurations of our designed metasurface.

Figure 4 shows photographs of the acoustic scanning test rig and associated measurement equipment. The metasurfaces are installed tightly between two parallel Plexiglas plates with dimensions of  $2400 \times 1200 \times 30 \text{ mm}^3$  (which guarantees that only the fundamental mode wave exists in the measured space). Wedge-shaped sound sponges are installed on the three sides to minimize the reflected acoustic waves. The incident plane wave is generated by a loudspeaker array of  $20 \times$  Pui Audio AS04008COR with 80 cm length. Two microphones (GRAS type 46BE), one static and one traveling, are utilized to scan the scattered region ( $80 \times 90 \text{ cm}^2$ ). The numbers of measured points are  $75 \times 68$  for an incident wave at 4000 Hz and  $75 \times 46$  for an incident wave at 3000 Hz. From the measured wave signal and the reference signal obtained from the static microphone, the transmitted sound fields produced by the metasurface are obtained.

## III. RESULTS AND DISCUSSION

In this section, we present five frequency-multiplexed designs corresponding to the distinct acoustic functionalities, including: two-frequency-multiplexed wave focusing at dual spatial points on the same focal plane; two-frequency-multiplexed acoustic function switching between wave steering and beam steering; off-axis three-frequency-multiplexed acoustic focusing on two different focal planes; three-frequency-multiplexed acoustic

focusing on three in-line planes with different depths of field; and three-frequency-multiplexed function switching between acoustic focusing and multidirection anomalous refraction.

### A. Two-frequency-multiplexed acoustic focusing

The design objective for this metasurface is to focus an acoustic wave of 3000 Hz at the spatial point (0.40 m, 0.1 m) and a wave of 4000 Hz at (0.40 m,  $-0.1$  m). Cross sections of the 16 optimized unit cells are shown in Fig. 5(a) and the corresponding 3D printed metasurface is shown in Fig. 5(d). The required phase shift calculated from Eq. (2) and the simulated phase shift of each metasurface unit are plotted in Fig. 5(c). It can be seen that the two sets of results agree with each other well at both frequencies. The largest difference of phase shifts is around  $7^\circ$ . The transmission coefficients of all designed unit cells are plotted in Fig. 5(d). All are larger than 0.75 and the average value is larger than 0.94, indicating that each unit cell is well optimized.

To evaluate the performance of the entire metasurface, the transmitted sound pressure fields corresponding to two incident waves with different operation frequencies are simulated. The simulated sound pressure field and the normalized intensity field corresponding to 3000 and 4000 Hz are plotted in Figs. 6(a) and 6(b), respectively. The focused points in both cases can be clearly seen in the pressure field as well as in the intensity field. From the two panels, the focus locations can be estimated, which are around (0.378 m, 0.0725 m) and (0.373 m,  $-0.108$  m) at 3000 and 4000 Hz, respectively. These locations are fairly close to the desired focal point. The normalized sound intensity field reveals the sharpness of the focusing and wave convergence phenomenon. The measured pressure fields of the two cases are plotted in Figs. 6(c) and 6(d). The focal points are found to be located at (0.379 m,  $-0.0675$  m) and (0.366 m, 0.125 m), which are quite close to the desired and simulated spatial positions.

To provide more quantitative results, Fig. 7 plots the normalized sound intensity and sound pressure level along the vertical line located at the focused point, that is,  $x = 0.378$  m for the case of 3000 Hz and  $x = 0.373$  m for the case of 4000 Hz. From these curves, the full width at half-maximum (FWHM) and the signal-to-noise ratio (SNR) can be used to analyze the performance of acoustic focusing and spatial resolution. At 3000 Hz, the FWHM is  $0.59\lambda$  and the SNR is 12.49 dB. The intensity of acoustic focusing reaches 2.35 times that of the incident plane wave. At 4000 Hz operation frequency, its spatial resolution is  $0.62\lambda$  and SNR is at 9.81 dB. The focusing strength becomes 2.94 times that of the incident plane wave. In addition, the measured sound pressure field demonstrates that the optimized frequency-multiplexed metasurface realizes acoustic focusing as desired—the measured FWHMs at 3000

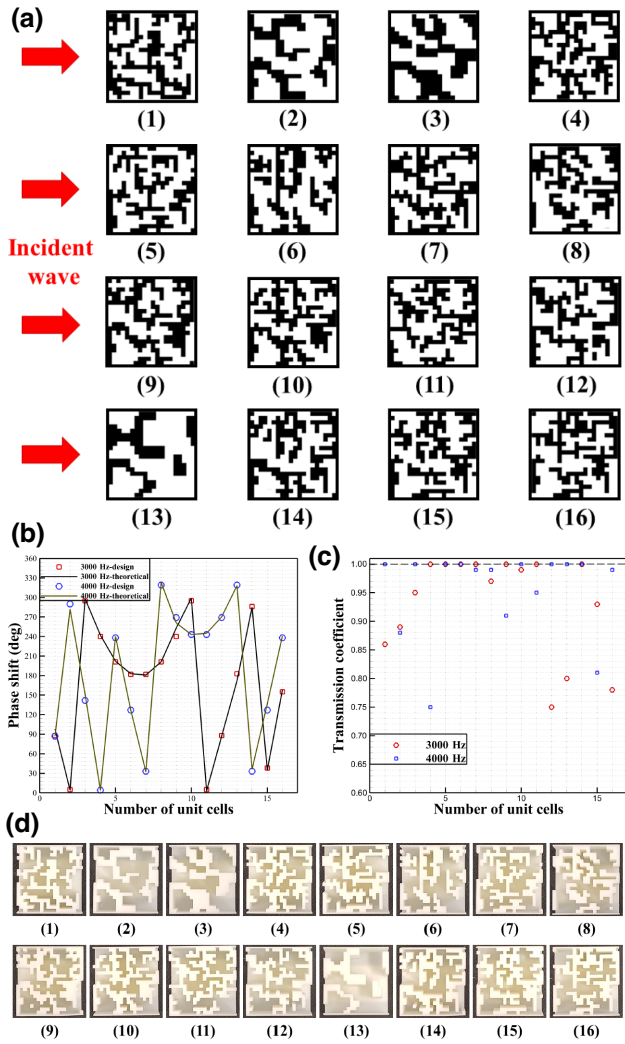


FIG. 5. The unit cells of the optimized metasurface for two-frequency-multiplexed wave focusing and their acoustic characteristics. (a) The cross section of each unit cell (black elements represent the solid materials, white elements are the air domain). (b) The phase shift of each unit cell and the corresponding desired value. (c) The transmission coefficient of each unit cell. (d) The 3D printed test samples (arrange from no. 1 to no. 16 to form the entire metasurface sample).

and 4000 Hz are  $0.62\lambda$  and  $0.58\lambda$ , respectively. Further improvement can be achieved by increasing the number of unit cells and the number of elements in each unit cell.

### B. Two-frequency-multiplexed function switching

In certain applications such as perception-operation integrated devices, it is desirable to have a system or device that can perform two distinct wave-front manipulation functions. As a demonstration, a passive metasurface that can perform wave focusing for a normally incident wave of 3000 Hz and wave steering for a normally incident wave of 4000 Hz is designed. The desired focusing

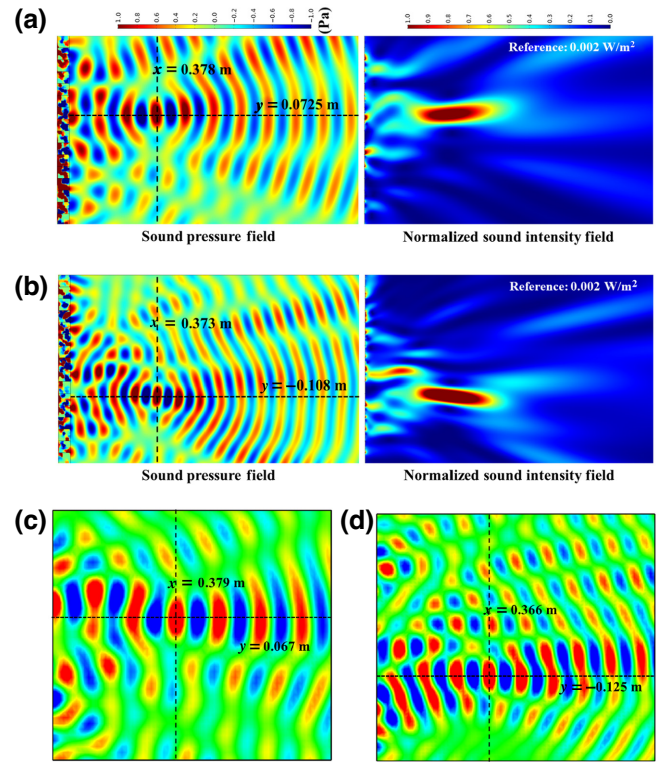


FIG. 6. The transmitted wave fields of normally incident plane waves through the designed metasurface for two-frequency-multiplexed wave focusing. (a) Simulated pressure and normalized intensity fields at 3000 Hz. (b) Simulated pressure and normalized intensity fields at 4000 Hz. (c) Measured sound pressure field at 3000 Hz. (d) Measured sound pressure field at 4000 Hz.

point is at  $(0.6$  m,  $0$  m), and the desired steering direction is the direction with an angle of refraction of  $12.40^\circ$ .

Again, the metasurface consists of 16 unit cells. The optimized designs of these unit cells, the fabricated metasurface test samples, and their acoustic characteristics are shown in Fig. 8. Compared with the desired values, the phase shift of each unit cell agrees well with the desired values, with the largest difference being  $10^\circ$ . Moreover, the transmission coefficients of all metasurface units are larger than 0.76 and the average value exceeds 0.96, guaranteeing a high transmitted sound energy. The results show that two different phase-shift profiles, i.e., linear and hyperbolic profiles, have been successfully encoded into one metasurface using the TO-based design approach. This allows it to have two distinct wave-front manipulation functions, and also provides the opportunity to design any multifunctional phase-gradient metasurface encoded with various acoustic functionalities, including Bessel beam generation, self-beading beam generation, and sound diffuser.

Figure 9 plots the sound fields transmitted through the designed metasurface. From the sound pressure field and

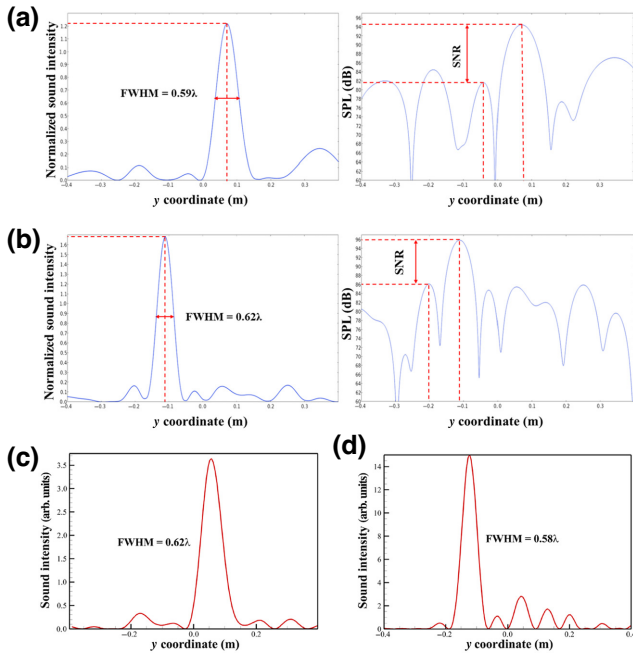


FIG. 7. Acoustic performance of the two-frequency-multiplexed focusing metasurface (FWHM and SNR): (a) wave focusing at 3000 Hz; (b) wave focusing at 4000 Hz; (c) measured focusing intensity at 3000 Hz; and (d) measured focusing intensity at 4000 Hz.

the normalized intensity field, it can be seen that the metasurface can focus the normally incident plane wave of 3000 Hz quite well. The observed focusing point on the pressure field is at (0.574 m, -0.0187 m). The measured pressure field shows a focal point at (0.537 m, -0.0103 m). Both are quite close to the desired location. For the beam steering function, the simulated pressure field at 4000 Hz shows that the main lobe of the transmitted sound wave is along the direction with an angle of refraction of 14.02°. However, there are also some high-order diffraction beams along other directions, which consume some wave energy. In this design case, most of these high-order diffraction beams would deteriorate rapidly without affecting the acoustic far field. A main reason for the presence of other wave components is that the metasurface is designed based on phase modulation only and the linear phase profile is realized, and the interference or crosstalk between two distinct acoustic functions has a negative effect.

From the measured sound field at 4000 Hz, the first-order refraction beam is along the direction of 13.89°. Similar to the simulation results, there also exist some other wave components in the measured field. It seems that the experimental results of beam steering are better than the simulation results, with less energy being radiated into other directions. A possible reason is that thermoviscous losses, which are not included in the simulation,

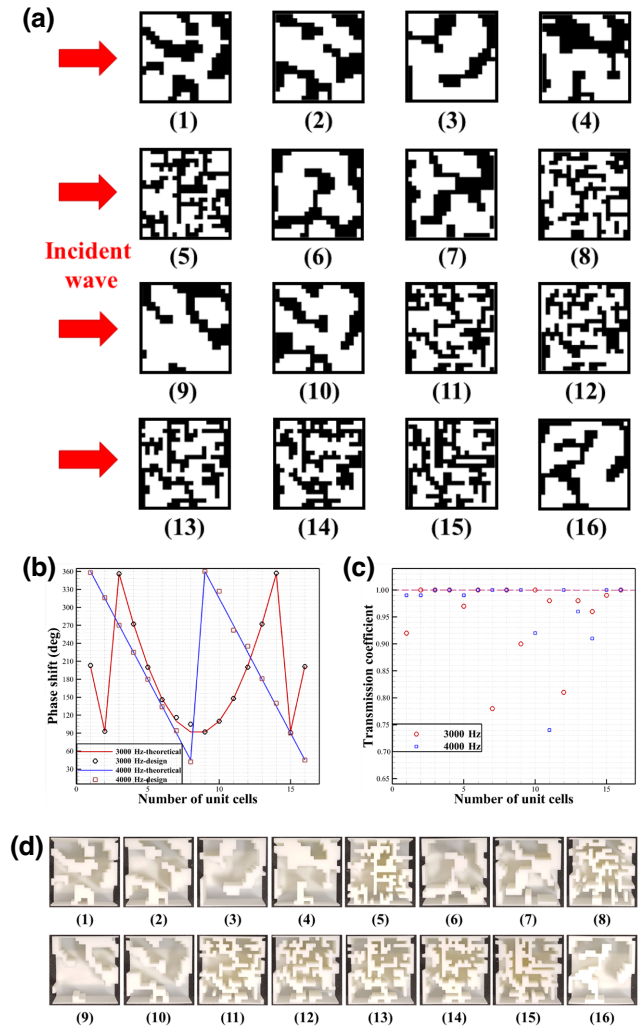


FIG. 8. The unit cells of the optimized metasurface for two-frequency-multiplexed function switching. (a) The cross section of the unit cells (black elements represent the solid materials, white elements are the air domain). (b) The phase shifts of the unit cells and the corresponding desired values. (c) The transmission coefficients of the unit cells. (d) The 3D printed test samples (arrange from no. 1 to no. 16 to form the entire metasurface sample).

can weaken the relatively weak near-field wave interaction to a certain extent, further hindering the propagation of high-order diffraction beams or even eliminate them.

The performance of the metasurface for acoustic focusing is further demonstrated in Figs. 10(a)–10(c), where the normalized sound intensity and the sound pressure level along the vertical line passing through the focusing point are plotted. The FWHMs of simulated and measured wave focusing show values of  $0.61\lambda$  and  $0.55\lambda$ , respectively. The SNR is 6.73 dB, and the focusing intensity reaches 1.92 times that of the incident wave, which is slightly lower than that in the previous design case. This indicates the high complexity of the design with two distinct functions

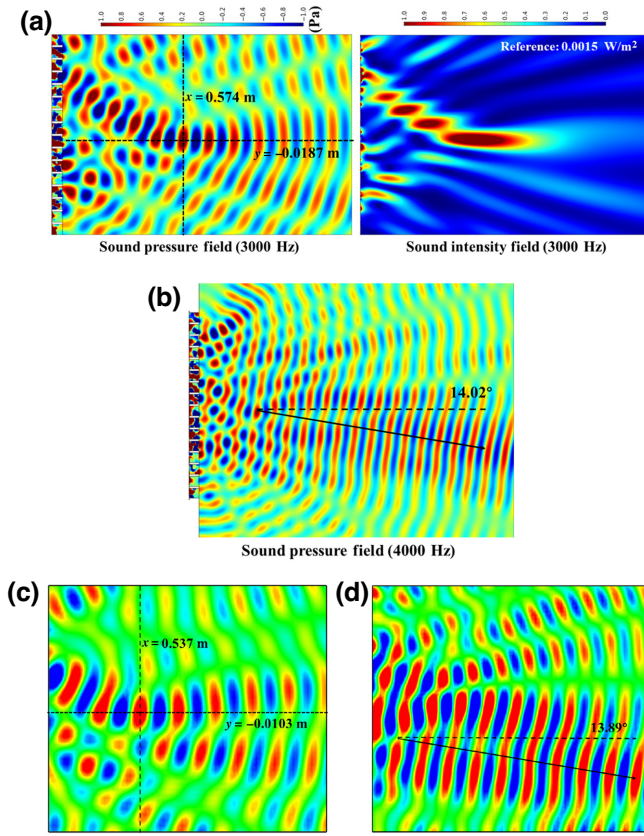


FIG. 9. The transmitted wave fields of normally incident plane waves through the designed metasurface for two-frequency-multiplexed function switching. (a) Simulated pressure and intensity fields at 3000 Hz (wave focusing). (b) Simulated pressure field at 4000 Hz (beam steering). (c) Measured sound pressure field of wave focusing at 3000 Hz. (d) Measured sound pressure field of beam steering at 4000 Hz.

as compared to the previous case. Figure 10(c) shows the polar plot for beam steering. From the plot, the directivity of the far-field sound wave at 4000 Hz is really evident.

### C. Physical mechanisms of frequency-multiplexed metasurfaces

To clarify the underlying physical mechanisms of multifunctional metasurfaces, we further study the detailed acoustic characteristics of the unit cells. According to the optimized structures of the unit cells, shown in Figs. 5(a) and 8(a), it is found that they can be roughly divided into two groups: blocklike structure and labyrinthlike structure. Among the unit cells in the two-frequency-multiplexed acoustic focusing metasurfaces, unit cells no. 2, no. 3, and no. 13 belong to blocklike structure, and the rest belong to labyrinthlike structure.

Figure 11(a) plots the normalized acoustic pressure fields (colored contours) and energy flux (arrowed lines) of an acoustic wave passing through three representative

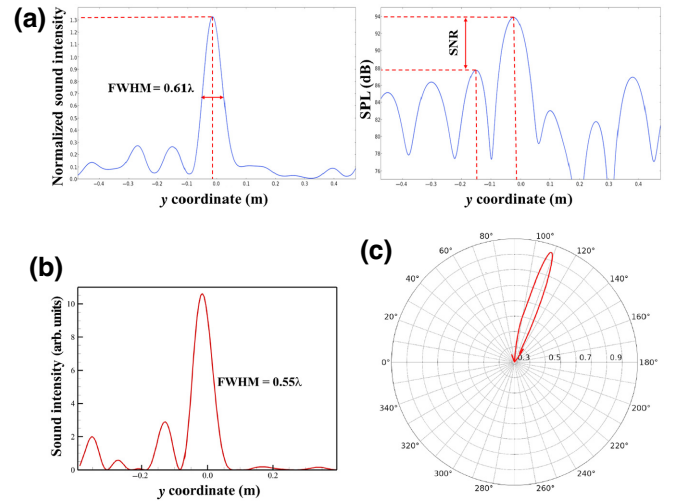


FIG. 10. Acoustic performance of the designed metasurface for two-frequency multiplexed function switching: (a) simulated FWHM and SNR at 3000 Hz; (b) measured wave focusing intensity at 3000 Hz; and (c) simulated far-field sound directivity at 4000 Hz.

blocklike unit cells. Because of the large difference in magnitude between the forward- and backward-propagating waves, the energy flux only indicates the acoustic propagation direction and energy gradient (similarly hereinafter). Compared with conventional space-coiling and helical structures, our optimized designs exhibit obviously asymmetric and complex structures. These structures cause the forward and backward waves to propagate along distinct paths inside the unit cells, resulting in different acoustic responses, such as phase shift and energy transmittance. As a result, our designs demonstrate the phenomena of asymmetric transmission and bianisotropy effect. To further verify this, the impedance spectrum (surface impedance matrix)  $\begin{bmatrix} Z_{11} & Z_{12} \\ Z_{21} & Z_{22} \end{bmatrix}$  of these unit cells is calculated based on the method described in Ref. [63] and plotted in Fig. 11(b). The fact that  $Z_{11} \neq Z_{22}$  clearly indicates the bianisotropy effect. Additionally, multiple passages on the interfaces of some unit cells also produce reverse energy flows to further achieve phase compensation in the near field, which is one of the distinct phenomena in our designs.

The pressure field, the energy flux, and the corresponding impedance spectra of representative labyrinthlike unit cells of the frequency-multiplexed wave focusing metasurface are plotted in Fig. 12. Phenomena such as backward acoustic energy flow and strong asymmetric transmission are also present in these unit cells. These unit cells have more tortuous and narrow channels, which provide more opportunities for multiple scattering and internal wave interaction, giving rise to far stronger intensity fields, which help to realize high transmission coefficient while achieving phase compensation (different from strong resonance). The dependence of wave scattering and interaction

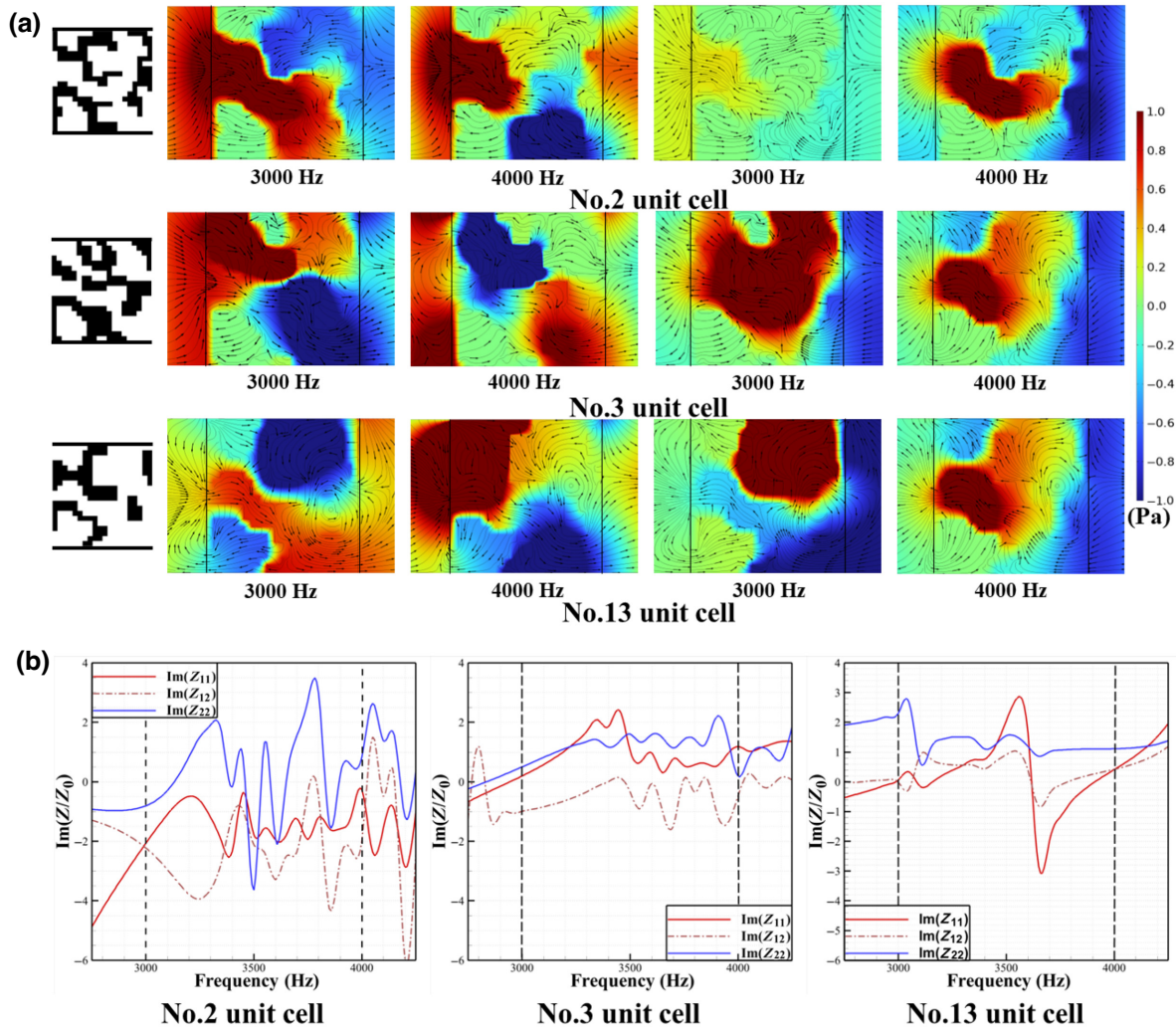


FIG. 11. Acoustic characteristics of three representative blocklike unit cells of the two-frequency-multiplexed acoustic focusing metasurface. (a) Normalized sound pressure fields and energy flux of forward (left two panels) and backward (right two panels) wave propagation. (b) Impedance spectra.

on the frequency produces distinct acoustic characteristics of waves with different operation frequencies, which helps to achieve different responses at 3000 and 4000 Hz. In other words, meticulously designed channels exert different roles in modulating waves with multiple operation frequencies to achieve the desired phase and transmittance responses. Additionally, there also exist weak local resonances [64] near either 3000 or 4000 Hz in some unit cells to assist in phase compensation through controlling energy flux.

The two-frequency-multiplexed function switching metasurface also contains blocklike structures, such as nos. 1–4, nos. 6–7, nos. 9–10, and no. 16, and labyrinthlike functional elements. Figures 13 and 14 present the pressure fields, energy flux, and impedance spectra of representative blocklike and labyrinthlike unit cells. The bianisotropy effect (asymmetric transmission),

multiple scattering, and weak local resonances near operation frequencies are still the dominant physical mechanisms of frequency-multiplexed wave manipulation, but the strength of wave coupling and wave-structure interaction becomes much stronger due to the narrower, tortuous sound channels. Unlike the previous bianisotropic design for asymmetric transmission devices [65], our results indicate that the bianisotropy effect can also be well utilized for achieving different acoustic functions in a passive metasurface.

Overall, the frequency-multiplexed properties of the designed metasurfaces are achieved through the bianisotropy effect, weak local resonances, and multiple wave-scattering and interaction effects. The tortuous structures promote the complex interaction between the acoustic waves and solid structures, and the multiple acoustic channels inspire strong wave coupling inside the unit cells.

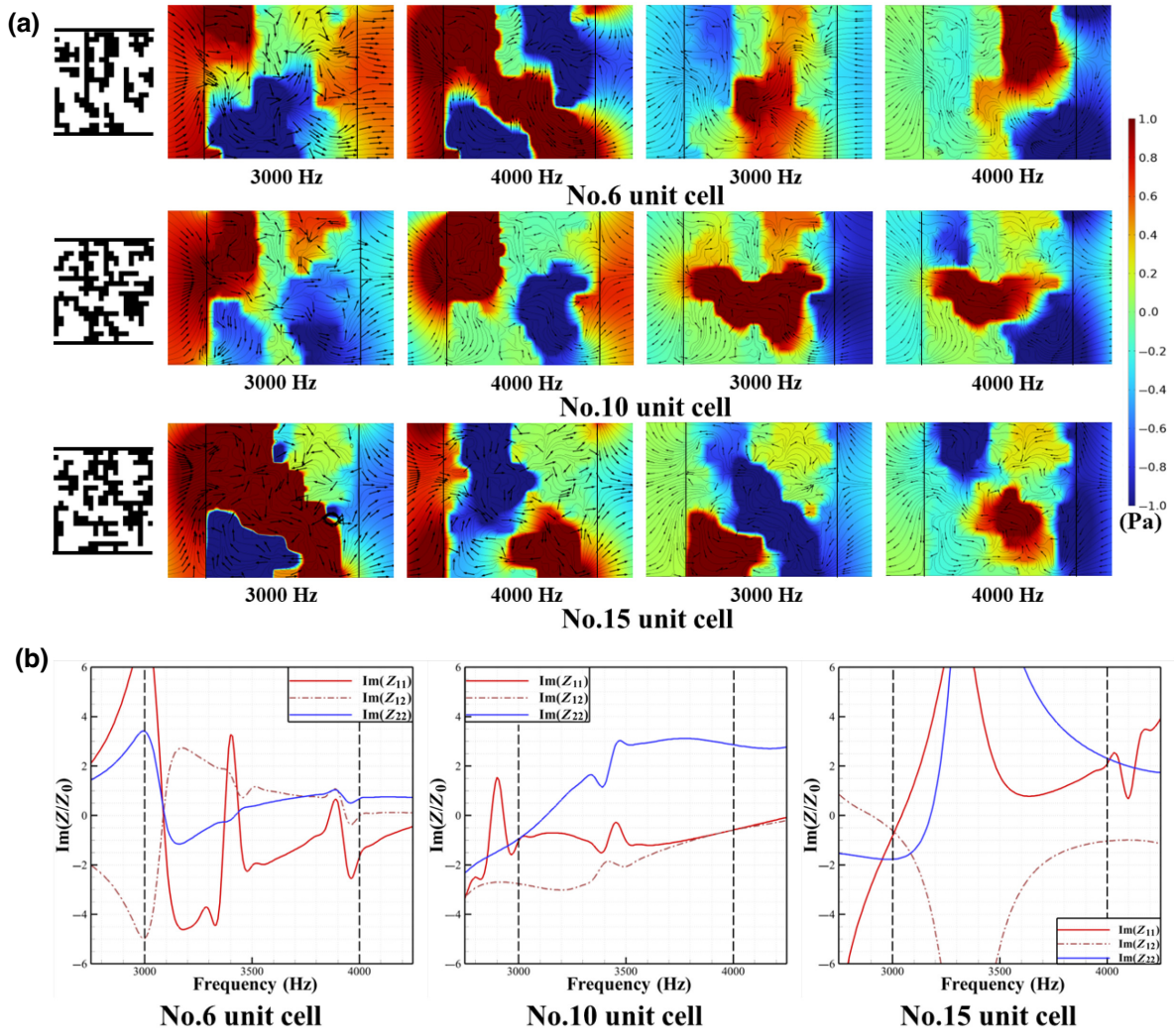


FIG. 12. Acoustic characteristics of three representative labyrinthlike unit cells of the two-frequency-multiplexed acoustic focusing metasurface. (a) Normalized sound pressure fields and energy flux of forward (left two panels) and backward (right two panels) wave propagation. (b) Impedance spectra.

These two features produce the desired phase shifts and high transmittance at different frequencies. The weak local resonances present near operation frequencies also contribute to the realization of phase compensation, but not in a dominant role.

It should be noted that these structure features are not separate from each other. They are integrated through the complex structure designs. For example, tortuous structures into local cavities and narrow channels not only promote strong multiple-scattering phenomena and internal wave interactions, but also increase the spatial degree of freedom to further realize more wave functionalities. Besides, forming multiple complex acoustic channels inspires the additional internal wave coupling and surface reverse energy flux, which further provides novel degree of freedom of acoustic-wave-front modulation. Compared with traditional microstructures designed using physics-driven approaches, like space-coiling, Helmholtz

and FP resonance, our optimized designs are more complex, allowing different physical mechanisms to be integrated together and utilized to realize complex functionalities.

#### D. Three-frequency-multiplexed off-axis focusing

Two-frequency-multiplexed metasurfaces are fundamental to multifunctional devices and can only realize limited wave functionalities. To address multiple channels of sound signals or information for more practical application scenarios, it is necessary to increase the number of operation frequencies to realize distinct acoustic functions. Because of stronger crosstalk among three distinct acoustic functions in a specific bandwidth, three-frequency-multiplexed wave manipulation with a metasurface is more challenging than two-frequency-multiplexed designs. There is not much work achieving

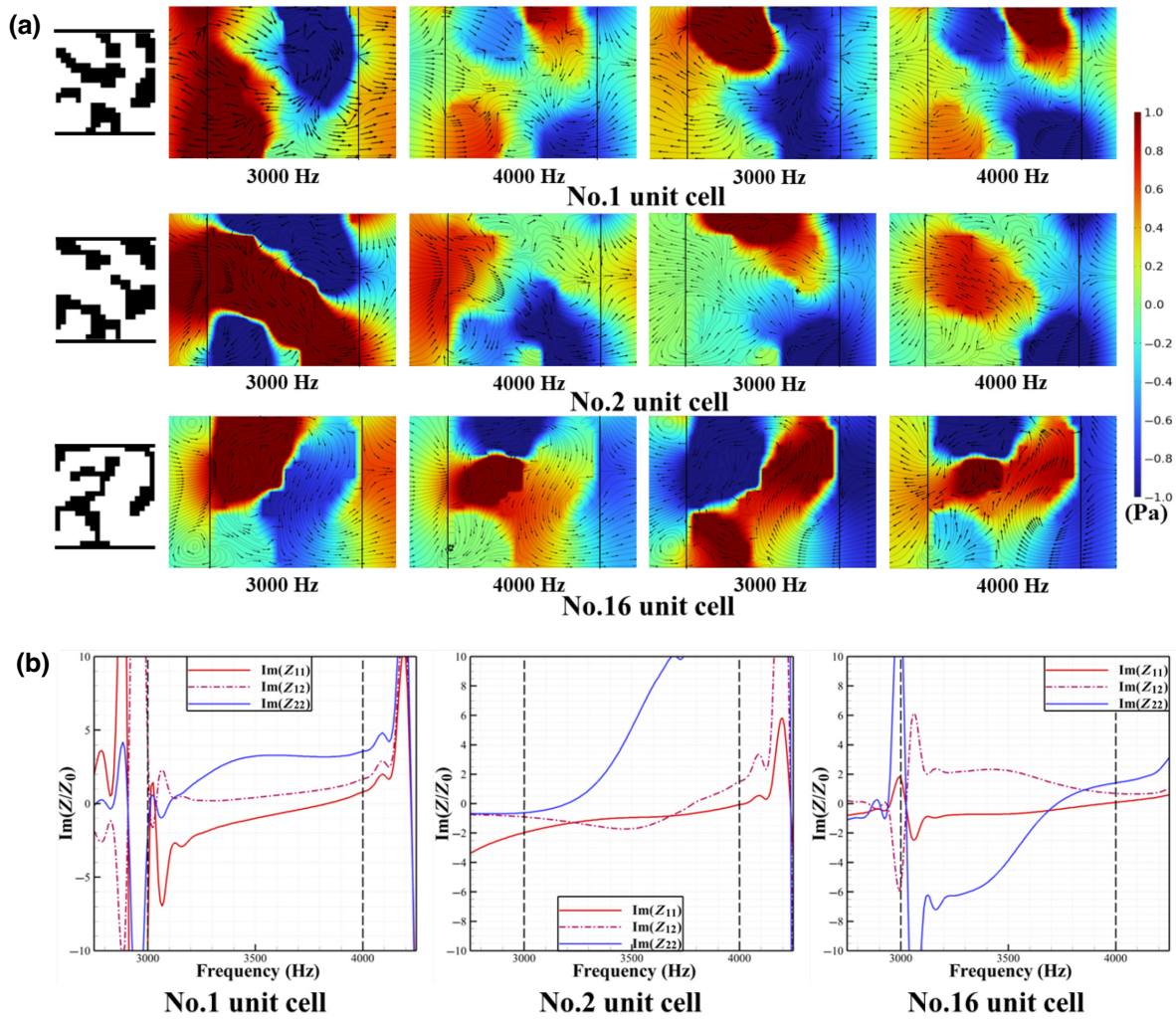


FIG. 13. Acoustic characteristics of three representative blocklike unit cells of the two-frequency-multiplexed function switching metasurface. (a) Normalized sound pressure fields and energy flux of forward (left two panels) and backward (right two panels) wave propagation. (b) Impedance spectra.

three-frequency-multiplexed transmission-type airborne metasurfaces. Therefore, to further broaden the applications of acoustic metasurfaces, we intend to design frequency-multiplexed acoustic metasurfaces for three functionalities at three operation frequencies, including off-axis wave focusing, in-line wave focusing, and function switching.

Three incident waves of 2500, 3500, and 4500 Hz are used and the corresponding target is a symmetric point at (0.7 m, 0 m), and a pair of confocal points at (0.5 m, 0.09 m) and (0.5 m, -0.09 m), respectively. It is possible to apply this type of acoustic metasurface mostly in imaging involving multiple fields of view and depths of field.

Again, a metasurface with 16 unit cells is designed. For a concise presentation here, the topological structures of each optimized unit cell and its corresponding acoustic characteristics are presented in the Appendix. Figure 15 shows the simulated transmitted sound pressure field and

normalized sound intensity of the incident wave of 2500 Hz. The spatial focal point appears at (0.663 m, 0 m), which is very close to the objective position. In detail, the FWHM and the SNR are estimated from Fig. 15(b), which are  $0.79\lambda$  and 7.91 dB, respectively. And the wave focusing strength is 1.70 times that of the incident wave. These results show that the incident acoustic energy is well concentrated on the vertical direction but spreads along the horizontal direction.

The focusing performance of the designed metasurface for the wave of 3500 Hz is shown in Fig. 16. The observed focal point from the pressure field shown in Fig. 16(a) is at (0.502 m, 0.063 m). The distances between this focal point and the target values in the horizontal and vertical directions are 0.002 m and 0.027 m, respectively. The desired signal in the focus region is 7.17 dB larger than the adjacent background sound. The spatial resolution of the acoustic focusing, FWHM is  $= 0.60\lambda$ , which is much

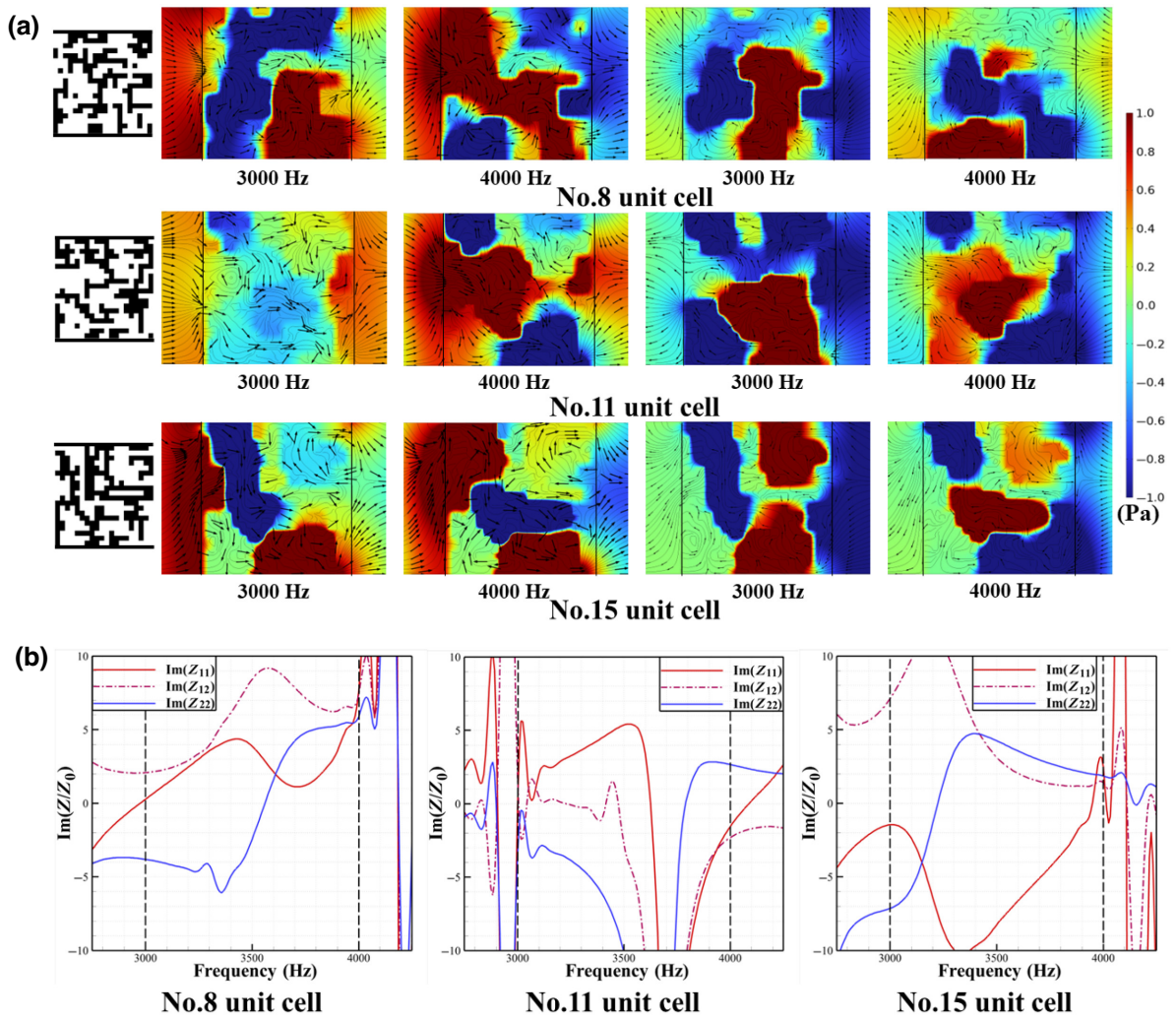


FIG. 14. Acoustic characteristics of three representative labyrinthlike unit cells of the two-frequency-multiplexed acoustic focusing metasurface. (a) Normalized sound pressure fields and energy flux of forward (left two panels) and backward (left two panels) wave propagation. (b) Impedance spectra.

better than that of 2500 Hz. The focusing strength is also better, which is 2.11 times that of the incident wave.

For the case with the incident wave of 4500 Hz, the estimated focusing point is at (0.497 m, -0.092 m) as shown in Fig. 17. Compared with the target point, it is about 0.003 m and 0.002 m away in the horizontal and vertical directions, respectively. The normalized wave focusing strength remains 2.57 times. In addition, our designed acoustic metasurface obtains the focusing resolution of  $0.71\lambda$  and the signal contrast near the focus area of 7.67 dB from Fig. 17(b).

### E. Three-frequency-multiplexed in-line focusing

As another example of a multifunctional metasurface realized with our inverse approach, a three-frequency-multiplexed metasurface is designed to achieve wave focusing on three different focal planes along the  $x$

axis. This designed metasurface can be utilized for high-capacity imaging with multiple depths of field. In this work, three desired focusing points are (0.5 m, 0 m), (0.6 m, 0 m), and (0.7 m, 0 m), which are realized using waves with 3000, 4000, and 4500 Hz, respectively. Because of the symmetry of the design, only half of the 16 unit cells are designed. The detailed topological structure of each optimized unit cell and its corresponding acoustic characteristics are also presented in the Appendix.

The simulated sound pressure fields and normalized intensity fields corresponding to three incident waves are plotted in Figs. 18(a), 19(a), and 20(a). For the incident wave of  $f = 3000$  Hz, the focal point appears at (0.522 m, -0.007 m), which is quite close to the target point. The spatial resolution of acoustic focusing estimated from Fig. 18(b) reaches  $0.58\lambda$ , and the contrast of focusing signal is 6.56 dB. The strength of wave focusing is 1.35 times that of the incident plane wave.

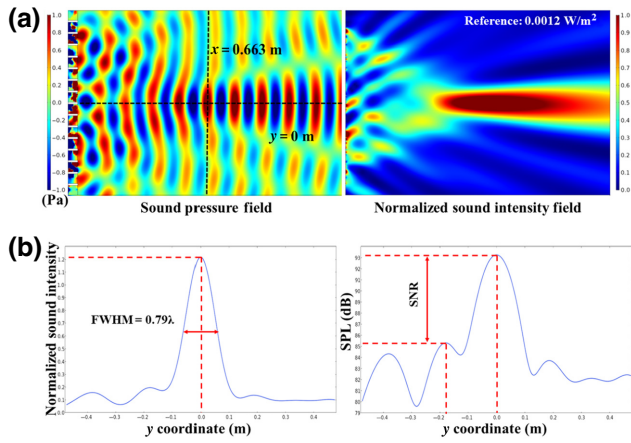


FIG. 15. Acoustic performance of the three-frequency-multiplexed metasurface for off-axis focusing at 2500 Hz: (a) simulated sound pressure and normalized intensity field; and (b) FWHM and SNR.

For the incident wave of  $f = 4000$  Hz, the plane wave has been concentrated on  $(0.61 \text{ m}, -0.023 \text{ m})$ , as shown in Fig. 19(a). From the normalized sound intensity and signal-to-noise ratio plotted in Fig. 19(b), the spatial resolution in the  $y$  direction is  $0.65\lambda$  and the SNR is  $6.01$  dB main-lobe signal strength. In addition, the designed metasurface realizes  $2.08$  times the acoustic focusing intensity at  $4000$  Hz operation frequency.

The focusing performance for the incident wave of  $4500$  Hz is not as good as that of the other two incident waves. A focusing point observed from the pressure and intensity plots in Fig. 20(a) is located at  $(0.677 \text{ m}, 0.012 \text{ m})$ , which is reasonably close to the designed focus. However, another strong focusing point appears closer to the metasurface, which consumes part of the sound energy and

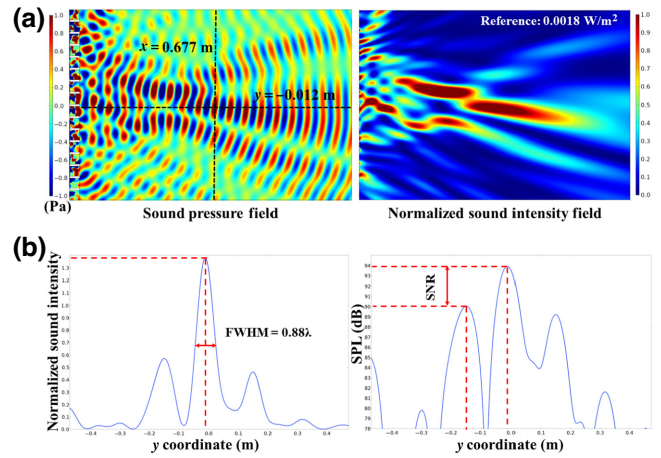


FIG. 17. Acoustic performance of the three-frequency-multiplexed metasurface for off-axis focusing at 4500 Hz: (a) simulated sound pressure and normalized intensity field; and (b) FWHM and SNR.

leads to a poor performance of the wave focusing function. The FWHM value is  $0.88\lambda$  and the SNR is only  $3.92$  dB, achieving  $1.98$  times focusing strength.

### F. Three-frequency-multiplexed function switching

In this section, we expand the two-frequency-multiplexed function switching metasurface into a three-frequency-multiplexed switching metasurface. The functions to be achieved are focusing the plane wave of  $3000$  Hz at spatial point  $(0.5 \text{ m}, 0 \text{ m})$ , and extraordinarily refracting the waves of  $4500$  and  $6000$  Hz to the directions along  $9.15^\circ$  and  $6.85^\circ$ , respectively (the phase gradient remains  $\pi/4$ , which is consistent with the two-frequency one). This kind of metadvice can potentially simultaneously realize

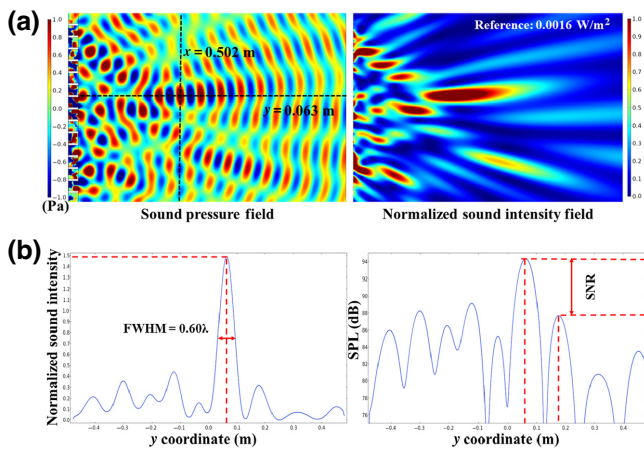


FIG. 16. Acoustic performance of the three-frequency-multiplexed metasurface for off-axis focusing at 3500 Hz: (a) simulated sound pressure and normalized intensity field; and (b) FWHM and SNR.

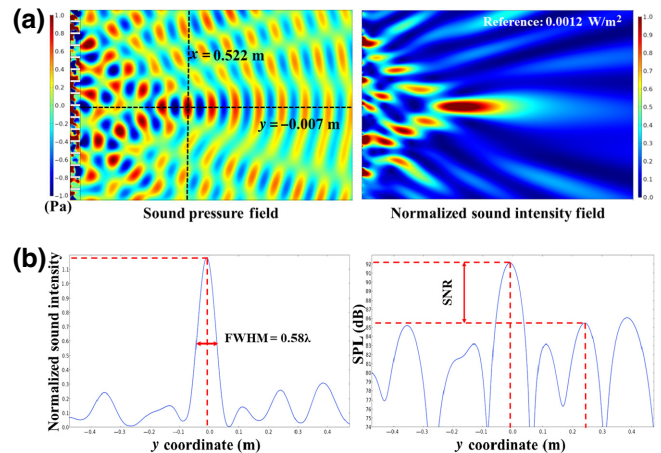


FIG. 18. Acoustic performance of the three-frequency-multiplexed metasurface for in-line focusing at 3000 Hz: (a) simulated sound pressure and normalized intensity field; and (b) FWHM and SNR.

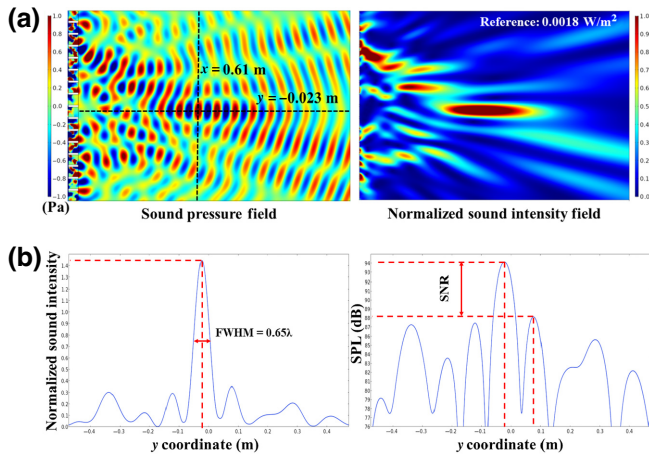


FIG. 19. Acoustic performance of the three-frequency-multiplexed metasurface for in-line focusing at 4000 Hz: (a) simulated sound pressure and normalized intensity field; and (b) FWHM and SNR.

acoustic imaging and multidirectional scanning or achieve the appropriate functions with dynamically switching various working frequencies, and probably further be applied in integrated multidirectional sector-scanning sound antenna and signal enhancement components.

Similarly, a metasurface containing 16 different unit cells is designed. For a detailed presentation, the topological structures of optimized metasurface units and their corresponding acoustic characteristics are indicated in the Appendix. Figure 21 provides the performance of wave focusing at 3000 Hz. The focal point appears at (0.471 m, -0.011 m) with 2.63 times focusing intensity and the spatial resolution can reach  $0.54\lambda$  with 4.28 dB signal contrast. For incident plane waves of 4500 and 6000

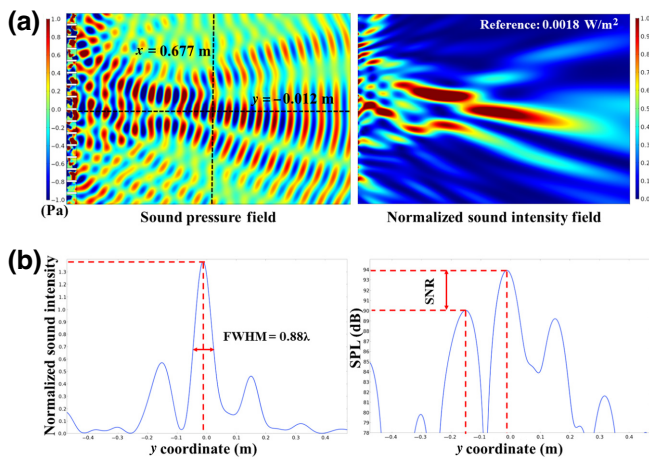


FIG. 20. Acoustic performance of the three-frequency-multiplexed metasurface for in-line focusing at 4500 Hz: (a) simulated sound pressure and normalized intensity field; and (b) FWHM and SNR.

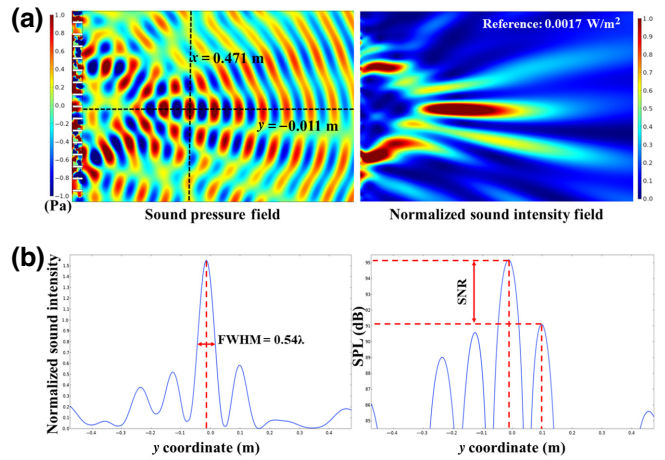


FIG. 21. Acoustic performance of the three-frequency-multiplexed metasurface for function switching at 3000 Hz: (a) simulated sound pressure and normalized intensity field; and (b) FWHM and SNR.

Hz, they transmit along  $10.25^\circ$  and  $-7.01^\circ$  directions through the designed metasurface (see Fig. 22). Because the wavelength of 6000 Hz is much closer to the aperture of designed unit cells (5 cm), there is much more sound energy scattering into undesired directions, which causes the first-order main beam to become much weaker. Decreasing the width of the unit cells can strengthen the intensity of the refraction beam to a certain extent with less energy scattering. It is noted that the thickness of our design (5 cm) remains subwavelength scale under all the operation frequencies, which demonstrates their potential in making compact, integrated, multifunctional acoustic devices.

Overall, by comprehensively analyzing the unit cells and entire metasurfaces for three-frequency-multiplexed acoustic functions, we find that, although the phase shifts and the transmission coefficients of each unit cell at different operation frequencies have achieved target values reasonably well, the performance of the entire metasurface is not as good as desired. There are two factors that may contribute to this.

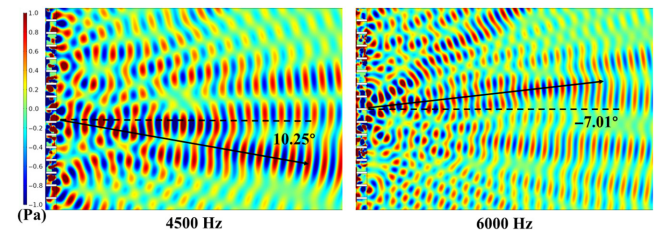


FIG. 22. Simulated sound pressure fields of three-frequency-multiplexed metasurface for function switching at 4500 and 6000 Hz.

One is the interference between two adjacent distinct functionalities. When the number of operation frequencies increases, there is more wave information that needs to be encoded into one passive metasurface and more strong crosstalk among multiplexed functionalities. With a small frequency gap, it is challenging to achieve corresponding delicate energy channeling for distinct acoustic functions, which will have serious mutual interference, worsening the sound performance at different frequencies. Hence, the solution to address this problem is to utilize waves with larger frequency differences or enlarge the thickness of the unit cell, which uses the spatial degree of freedom in exchange for the energy degree of freedom.

Another influence factor is the near-field wave coupling effect. According to Sec. III C, some optimized unit cells may indicate energy backflow near the interfaces at certain frequencies, which probably gives rise to unexpected complex energy coupling along the surface of metasurfaces. Parts of the sound energy is radiated into other directions in the form of high-order waves, or left in the near-field region in the form of evanescent waves, and further reduce the power efficiency of the corresponding acoustic functionality. To improve this situation, nonlocal metasurface design seems a potential approach.

#### IV. CONCLUSIONS

In this paper, we present a design framework based on the multiobjective gradient-free topology optimization method for the design of ultrathin, passive, multifunctional transmission-type acoustic metasurfaces. These metasurfaces are capable of manipulating wave fronts with different frequencies by encoding distinct phase profiles or functionalities onto one single design. Compared to a conventional physics-driven design method, the proposed design methodology is more systematic and suitable for designing high-performance metasurfaces with multiple objectives and constraints, and without human intervention.

We have designed several two-frequency- and three-frequency-multiplexed metasurfaces for acoustic coplanar focusing and function switching. Their wave control performances have been evaluated through numerical simulations and experimental measurements. By analyzing the underlying physical mechanisms, we have found that different phase profiles are achieved through frequency-dependent mechanisms such as bianisotropy, multiple scattering, multiple acoustic channels, and weak local resonance. The inverse design approach automatically selects and seamlessly integrates the most suitable topological structures and physical mechanisms for each design task, depending on the operation frequency.

The design challenge is to realize different phase profiles on the same design. If the phase profiles are vastly different from each other, and if more phase profiles are to be encoded, the design will be more difficult. To ensure

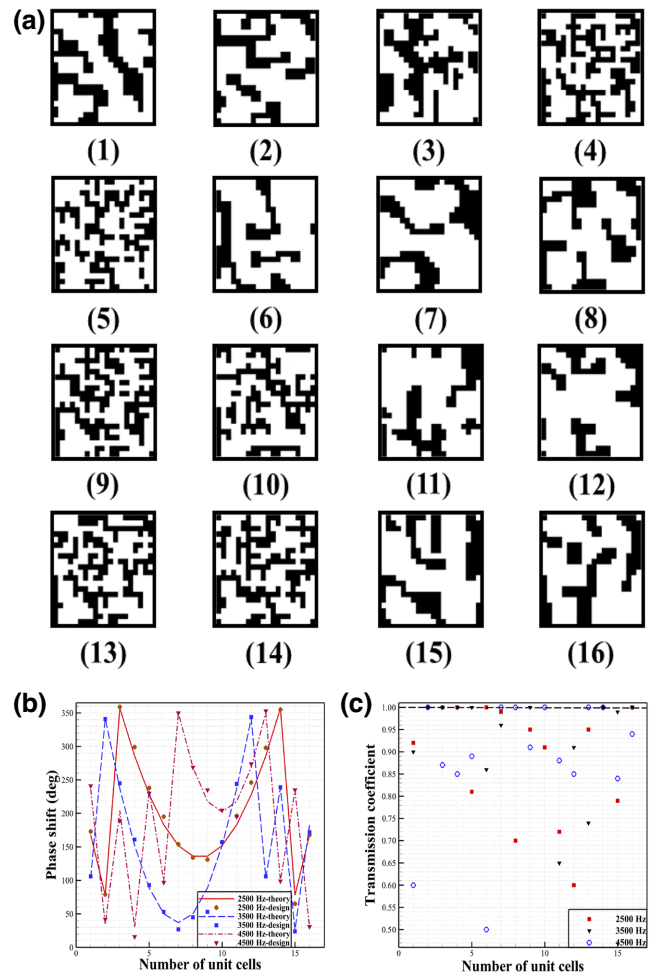


FIG. 23. The unit cells of the optimized metasurface for three-frequency-multiplexed off-axis wave focusing and their acoustic characteristics. (a) The cross section of each unit cell (black elements represent the solid materials, white elements are the air domain). (b) The phase shifts of the unit cells and the corresponding desired values. (c) The transmission coefficients of the unit cells.

good performance, one should choose incident waves with a relatively large frequency gap. Additionally, one should allow sufficient design elements and/or variables in each unit cell. Our results demonstrate that the proposed design framework opens an avenue to develop high-performance, compact, integrated, multifunctional acoustic components and devices.

It should be pointed out that the GSL design principle is based only on the phase gradient, without considering the impedance matching inside the metasurface and on the interfaces between the metasurface and background media (amplitude or energy), which cause undesired sound energy reflection and/or scattering and near-field coupling. Therefore, in our future work, we will adopt the impedance-based approach to achieve multifunctional acoustic metadevices with high energy efficiency.

ACKNOWLEDGMENTS

This work is in part supported by the Hong Kong Research Grants Council under Competitive Earmarked Research Grant No. 16212318 and 16206320. The authors would like to sincerely thank Hongjun Lin for fruitful discussions and Junjie Rong for highly valuable comments and constructive suggestions to improve the research.

APPENDIX: TOPOLOGICAL STRUCTURES OF THREE-FREQUENCY-MULTIPLEXED METASURFACES

The detailed structures and acoustic characteristics of 16 unit cells of three-frequency-multiplexed metasurfaces for off-axis wave focusing are shown in Fig. 23. Their phase shifts produced by the incident plane waves of 2500 and 4500 Hz agree well with theoretical values. For the incident wave of 3500 Hz, the agreement between the phase shifts produced and the expected values is mostly good except for a couple of the unit cells. Most transmission coefficients are larger than 0.80 and the average transmission value of each operation frequency is 0.91, 0.88, and 0.86, respectively.

The topological structures and acoustic characteristics of eight functional elements of a three-frequency-multiplexed metasurface for in-line wave focusing are shown in Fig. 24. All the transmission coefficients are

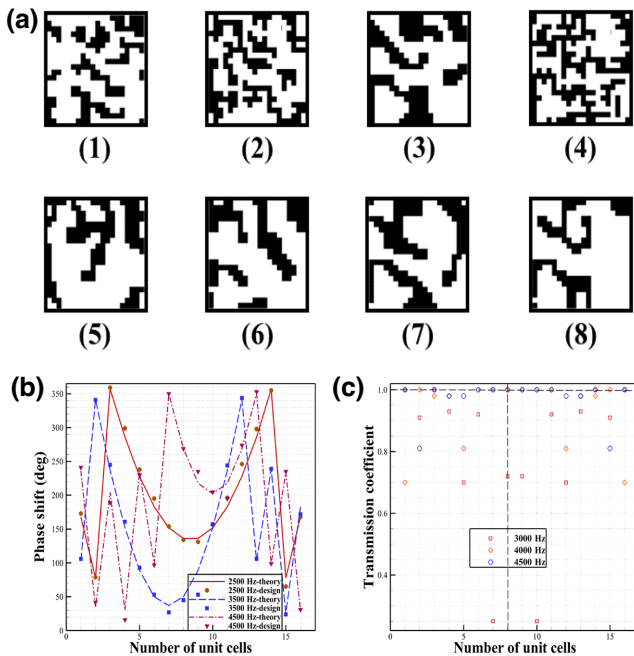


FIG. 24. The unit cells of the optimized metasurface for three-frequency-multiplexed in-line wave focusing and their acoustic characteristics. (a) The cross section of each unit cell (black elements represent the solid materials, white elements are the air domain). (b) The phase shifts of the unit cells and the corresponding desired values. (c) The transmission coefficients of the unit cells.

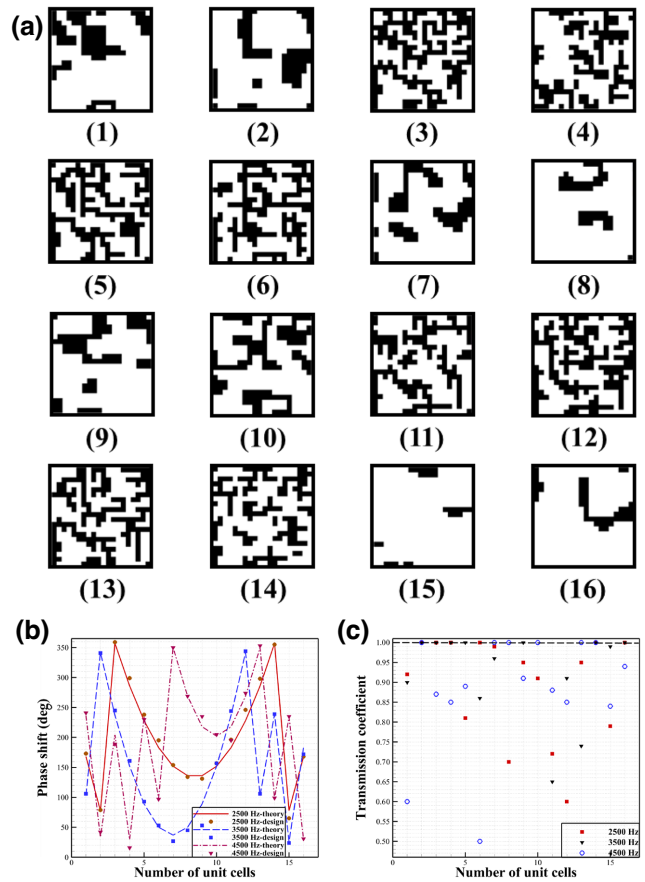


FIG. 25. The unit cells of the optimized metasurface for three-frequency-multiplexed function switching and their acoustic characteristics. (a) The cross section of each unit cell (black elements represent the solid materials, white elements are the air domain). (b) The phase shifts of the unit cells and the corresponding desired values. (c) The transmission coefficients of the unit cells.

beyond 0.7, and the phase profiles fit to the target ones well except for a few unit cells in the case with the incident wave of 4500 Hz, the maximum error of which is  $16^\circ$ .

Figure 25 provides the configuration of the unit cells, the corresponding phase shifts, and transmission coefficient performance of three-frequency-multiplexed function switching. The largest gap between theoretical and designed phase is  $12^\circ$ , and the others are all smaller than  $10^\circ$  to guarantee the high accuracy of phase profiles under three operation frequencies. In addition, the three average transmission coefficients are all larger than 0.9. However, the uniformity of transmission coefficient in the case with the incident wave of 3000 Hz seems slightly lower than in the other two conditions.

[1] A. Ozcelik, J. Rufo, F. Guo, Y. Gu, P. Li, J. Lata, and T. J. Huang, Acoustic tweezers for the life sciences, *Nat. Methods* 15, 1021 (2018).

- [2] A. Marzo and B. W. Drinkwater, Holographic acoustic tweezers, *Proc. Natl. Acad. Sci.* **116**, 84 (2019).
- [3] Z. Ma, A. W. Holle, K. Melde, T. Qiu, K. Poeppel, V. M. Kadiri, and P. Fischer, Acoustic holographic cell patterning in a biocompatible hydrogel, *Adv. Mater.* **32**, 1904181 (2020).
- [4] K. K. Amireddy, K. Balasubramaniam, and P. Rajagopal, Deep subwavelength ultrasonic imaging using optimized hole structured metamaterials, *Sci. Rep.* **7**, 1 (2017).
- [5] K. K. Amireddy, K. Balasubramaniam, and P. Rajagopal, Porous metamaterials for deep sub-wavelength ultrasonic imaging, *Appl. Phys. Lett.* **113**, 124102 (2018).
- [6] Y.-F. Zhou, High intensity focused ultrasound in clinical tumor ablation, *World J. Clin. Oncol.* **2**, 8 (2011).
- [7] Z. Izadifar, Z. Izadifar, D. Chapman, and P. Babyn, An introduction to high intensity focused ultrasound: Systematic review on principles, devices, and clinical applications, *J. Clin. Med.* **9**, 460 (2020).
- [8] Z. Qiu, S. Kala, J. Guo, Q. Xian, J. Zhu, T. Zhu, X. Hou, K. F. Wong, M. Yang, and H. Wang, *et al.*, Targeted neurostimulation in mouse brains with non-invasive ultrasound, *Cell Rep.* **32**, 108033 (2020).
- [9] S. L. Norman, D. Maresca, V. N. Christopoulos, W. S. Griggs, C. Demene, M. Tanter, M. G. Shapiro, and R. A. Andersen, Single-trial decoding of movement intentions using functional ultrasound neuroimaging, *Neuron* **109**, 1554 (2021).
- [10] T. Fushimi, A. Marzo, B. W. Drinkwater, and T. L. Hill, Acoustophoretic volumetric displays using a fast-moving levitated particle, *Appl. Phys. Lett.* **115**, 064101 (2019).
- [11] T. Fushimi, B. W. Drinkwater, and T. L. Hill, What is the ultimate capability of acoustophoretic volumetric displays?, *Appl. Phys. Lett.* **116**, 244101 (2020).
- [12] F. Li and R. Hu, Metamaterials-enabled sensing for human-machine interfacing, *Sensors* **21**, 161 (2020).
- [13] S. Pyo, J. Lee, K. Bae, S. Sim, and J. Kim, Recent progress in flexible tactile sensors for human-interactive systems: From sensors to advanced applications, *Adv. Mater.* **33**, 2005902 (2021).
- [14] C. Shi, M. Dubois, Y. Wang, and X. Zhang, High-speed acoustic communication by multiplexing orbital angular momentum, *Proc. Natl. Acad. Sci.* **114**, 7250 (2017).
- [15] X. Jiang, B. Liang, J.-C. Cheng, and C.-W. Qiu, Twisted acoustics: Metasurface-enabled multiplexing and demultiplexing, *Adv. Mater.* **30**, 1800257 (2018).
- [16] B. Liu, X. Chen, H. Cai, M. M. Ali, X. Tian, L. Tao, Y. Yang, and T. Ren, Surface acoustic wave devices for sensor applications, *J. Semicond.* **37**, 021001 (2016).
- [17] P. Delsing, A. N. Cleland, M. J. Schuetz, J. Knörzer, G. Giedke, J. I. Cirac, K. Srinivasan, M. Wu, K. C. Balram, and C. Bäuerle, *et al.*, The 2019 surface acoustic waves roadmap, *J. Phys. D: Appl. Phys.* **52**, 353001 (2019).
- [18] S. Zuo, Y. Tian, Y. Cheng, M. Deng, N. Hu, and X. Liu, Asymmetric coding metasurfaces for the controllable projection of acoustic images, *Phys. Rev. Mater.* **3**, 065204 (2019).
- [19] X. Jiang, H. Zhao, C. Zhang, J. He, Y. Li, B. Li, and D. Ta, Nondestructive evaluation of special defects based on ultrasound metasurface, *Front. Mater.* **8**, 802001 (2022).
- [20] M. Li, J. H. Wu, and X. Y. Yuan, Metasurface zero-impedance matching mechanism for aerodynamic noise reduction, *J. Sound Vib.* **536**, 117147 (2022).
- [21] J. Guo, Y. Fang, R. Qu, Q. Liu, and X. Zhang, An extra-broadband compact sound-absorbing structure composing of double-layer resonator with multiple perforations, *J. Acoust. Soc. Am.* **150**, 1370 (2021).
- [22] J. Guo, X. Zhang, Y. Fang, and R. Qu, An extremely-thin acoustic metasurface for low-frequency sound attenuation with a tunable absorption bandwidth, *Int. J. Mech. Sci.* **213**, 106872 (2022).
- [23] S.-W. Fan, S.-D. Zhao, L. Cao, Y. Zhu, A.-L. Chen, Y.-F. Wang, K. Donda, Y.-S. Wang, and B. Assouar, Reconfigurable curved metasurface for acoustic cloaking and illusion, *Phys. Rev. B* **101**, 024104 (2020).
- [24] H.-T. Zhou, W.-X. Fu, Y.-F. Wang, Y.-S. Wang, V. Laude, and C. Zhang, Ultra-broadband passive acoustic metasurface for wide-angle carpet cloaking, *Mater. Des.* **199**, 109414 (2021).
- [25] Y. Zhu, X. Fan, B. Liang, J. Cheng, and Y. Jing, Ultrathin Acoustic Metasurface-Based Schroeder Diffuser, *Phys. Rev. X* **7**, 021034 (2017).
- [26] W. K. Cao, L. T. Wu, C. Zhang, J. C. Ke, Q. Cheng, and T. J. Cui, A reflective acoustic meta-diffuser based on the coding meta-surface, *J. Appl. Phys.* **126**, 194503 (2019).
- [27] J. Chen, J. Rao, D. Lisevych, and Z. Fan, Broadband ultrasonic focusing in water with an ultra-compact metasurface lens, *Appl. Phys. Lett.* **114**, 104101 (2019).
- [28] X. Jiang, Y. Li, D. Ta, and W. Wang, Ultrasonic sharp autofocusing with acoustic metasurface, *Phys. Rev. B* **102**, 064308 (2020).
- [29] X.-F. Zhu and S.-K. Lau, Perfect anomalous reflection and refraction with binary acoustic metasurfaces, *J. Appl. Phys.* **126**, 224504 (2019).
- [30] L. Quan and A. Alù, Passive Acoustic Metasurface with Unitary Reflection Based on Nonlocality, *Phys. Rev. Appl.* **11**, 054077 (2019).
- [31] Z. Guo, H. Liu, H. Zhou, K. Zhou, S. Wang, F. Shen, Y. Gong, J. Gao, S. Liu, and K. Guo, High-order acoustic vortex field generation based on a metasurface, *Phys. Rev. E* **100**, 053315 (2019).
- [32] X. Jiang, D. Ta, and W. Wang, Modulation of Orbital-Angular-Momentum Symmetry of Nondiffractive Acoustic Vortex Beams and Realization Using a Metasurface, *Phys. Rev. Appl.* **14**, 034014 (2020).
- [33] B. Yuan, Y. Cheng, and X. Liu, Conversion of sound radiation pattern via gradient acoustic metasurface with space-coiling structure, *Appl. Phys. Express* **8**, 027301 (2015).
- [34] R. Ghaffarivardavagh, J. Nikolajczyk, R. Glynn Holt, S. Anderson, and X. Zhang, Horn-like space-coiling metamaterials toward simultaneous phase and amplitude modulation, *Nat. Commun.* **9**, 1 (2018).
- [35] T. Frenzel, J. David Brehm, T. Bückmann, R. Schittny, M. Kadic, and M. Wegener, Three-dimensional labyrinthine acoustic metamaterials, *Appl. Phys. Lett.* **103**, 061907 (2013).
- [36] C. Zhang and X. Hu, Three-Dimensional Single-Port Labyrinthine Acoustic Metamaterial: Perfect Absorption

- with Large Bandwidth and Tunability, *Phys. Rev. Appl.* **6**, 064025 (2016).
- [37] Y.-F. Tang, B. Liang, J. Yang, J. Yang, and J.-c. Cheng, Voltage-controlled membrane-type active acoustic metasurfaces with ultrathin thickness, *Appl. Phys. Express* **12**, 064501 (2019).
- [38] P. Liu, X. Chen, W. Xu, and Y. Pei, Magnetically controlled multifunctional membrane acoustic metasurface, *J. Appl. Phys.* **127**, 185104 (2020).
- [39] Y. Zhu and B. Assouar, Multifunctional acoustic metasurface based on an array of Helmholtz resonators, *Phys. Rev. B* **99**, 174109 (2019).
- [40] G.-S. Liu, Y.-Y. Peng, M.-H. Liu, X.-Y. Zou, and J.-C. Cheng, Broadband acoustic energy harvesting metasurface with coupled Helmholtz resonators, *Appl. Phys. Lett.* **113**, 153503 (2018).
- [41] M. D. Brown, B. T. Cox, and B. E. Treeby, Design of multi-frequency acoustic kinoforms, *Appl. Phys. Lett.* **111**, 244101 (2017).
- [42] Y. Zhu, N. J. Gerard, X. Xia, G. C. Stevenson, L. Cao, S. Fan, C. M. Spadaccini, Y. Jing, and B. Assouar, Systematic design and experimental demonstration of transmission-type multiplexed acoustic metaholograms, *Adv. Funct. Mater.* **31**, 2101947 (2021).
- [43] Y. Zhang, H. Cheng, J. Tian, and S. Chen, Frequency-Selected Bifunctional Coding Acoustic Metasurfaces, *Phys. Rev. Appl.* **14**, 064057 (2020).
- [44] Q. Chen, X. Zhang, and B. Zhu, Design of buckling-induced mechanical metamaterials for energy absorption using topology optimization, *Struct. Multidiscipl. Optim.* **58**, 1395 (2018).
- [45] Y. Zheng, Y. Wang, X. Lu, Z. Liao, and J. Qu, Evolutionary topology optimization for mechanical metamaterials with auxetic property, *Int. J. Mech. Sci.* **179**, 105638 (2020).
- [46] H.-W. Dong, S.-D. Zhao, Y.-S. Wang, and C. Zhang, Topology optimization of anisotropic broadband double-negative elastic metamaterials, *J. Mech. Phys. Solids* **105**, 54 (2017).
- [47] X. Yang and Y. Y. Kim, Topology optimization for the design of perfect mode-converting anisotropic elastic metamaterials, *Compos. Struct.* **201**, 161 (2018).
- [48] J. Andkjær and O. Sigmund, Topology optimized cloak for airborne sound, *J. Vib. Acoust.* **135**, 041011 (2013).
- [49] A. H. Bokhari, A. Mousavi, B. Niu, and E. Wadbro, Topology optimization of an acoustic diode?, *Struct. Multidiscipl. Optim.* **63**, 2739 (2021).
- [50] J. Guo, X. Zhang, and Y. Fang, Topology optimization design and experimental validation of an acoustic metasurface for reflected wavefront modulation, *J. Sound Vib.* **520**, 116631 (2022).
- [51] Z. Li, Y. Ke, G. Wu, and M. Tao, Topology optimization combined with a genetic algorithm to design structured materials for underwater broadband acoustic absorption, *J. Vib. Control* (2022).
- [52] S.-D. Zhao, H.-W. Dong, X.-B. Miao, Y.-S. Wang, and C. Zhang, Broadband Coding Metasurfaces with 2-Bit Manipulations, *Phys. Rev. Appl.* **17**, 034019 (2022).
- [53] X. L. Sun, J. P. Yan, Y. F. Li, and H. Liu, Multi-frequency ultrasound transducers for medical applications: A survey, *Int. J. Intell. Robot. Appl.* **2**, 296 (2018).
- [54] R. Hirayama, D. Martinez Plasencia, N. Masuda, and S. Subramanian, A volumetric display for visual tactile and audio presentation using acoustic trapping, *Nature* **575**, 320 (2019).
- [55] J. Chan, Z. Zheng, K. Bell, M. Le, P. H. Reza, and J. T. Yeow, Photoacoustic imaging with capacitive micro-machined ultrasound transducers: Principles and developments, *Sensors* **19**, 3617 (2019).
- [56] F. Depasse, M. Paesler, D. Courjon, and J. Vigoureux, Huygens–Fresnel principle in the near field, *Opt. Lett.* **20**, 234 (1995).
- [57] N. Yu, P. Genevet, M. A. Kats, F. Aieta, J.-P. Tetienne, F. Capasso, and Z. Gaburro, Light propagation with phase discontinuities: Generalized laws of reflection and refraction, *Science* **334**, 333 (2011).
- [58] K. Deb, A. Pratap, S. Agarwal, and T. Meyarivan, A fast and elitist multiobjective genetic algorithm: NSGA-II, *IEEE Trans. Evol. Comput.* **6**, 182 (2002).
- [59] Z. Li, R. Pestourie, Z. Lin, S. G. Johnson, and F. Capasso, Empowering metasurfaces with inverse design: Principles and applications, *ACS Photonics* **9**, 2178 (2022).
- [60] J. Black, N. Hashimzade, and G. Myles, *A Dictionary of Economics* (Oxford University Press, 2012).
- [61] H.-W. Dong, C. Shen, S.-D. Zhao, W. Qiu, H. Zheng, C. Zhang, S. A. Cummer, Y.-S. Wang, D. Fang, and L. Cheng, Achromatic metasurfaces by dispersion customization for ultra-broadband acoustic beam engineering, *Natl. Sci. Rev.* **9**, nwac030 (2022).
- [62] B. H. Song and J. S. Bolton, A transfer-matrix approach for estimating the characteristic impedance and wave numbers of limp and rigid porous materials, *J. Acoust. Soc. Am.* **107**, 1131 (2000).
- [63] A. Díaz-Rubio and S. A. Tretyakov, Acoustic metasurfaces for scattering-free anomalous reflection and refraction, *Phys. Rev. B* **96**, 125409 (2017).
- [64] J. Li, C. Shen, A. Díaz-Rubio, S. A. Tretyakov, and S. A. Cummer, Systematic design and experimental demonstration of bianisotropic metasurfaces for scattering-free manipulation of acoustic wavefronts, *Nat. Commun.* **9**, 1342 (2018).
- [65] A. Song, J. Li, X. Peng, C. Shen, X. Zhu, T. Chen, and S. A. Cummer, Asymmetric Absorption in Acoustic Metamirror Based on Surface Impedance Engineering, *Phys. Rev. Appl.* **12**, 054048 (2019).